JCI insight

RESEARCH ARTICLE

NELL-1 induces Sca-1$^+$ mesenchymal progenitor cell expansion in models of bone maintenance and repair

Aaron W. James,[1,2] Jia Shen,[3] Rebecca Tsuei,[3] Alan Nguyen,[3] Kevork Khadarian,[3] Carolyn A. Meyers,[1] Hsin Chuan Pan,[3] Weiming Li,[4] Jin H. Kwak,[3] Greg Asatrian,[3] Cymbeline T. Culiat,[5] Min Lee,[6] Kang Ting,[3] Xinli Zhang,[3] and Chia Soo[2,7]

[1]Department of Pathology, Johns Hopkins University, Baltimore, Maryland, USA. [2]UCLA and Orthopaedic Hospital Department of Orthopaedic Surgery and the Orthopaedic Hospital Research Center, Los Angeles, California, USA. [3]Division of Growth and Development and Section of Orthodontics, School of Dentistry, UCLA, Los Angeles, USA. [4]Department of Orthopedics, The First Clinical Affiliated Hospital of Harbin Medical University, Harbin, Heilongjiang, China. [5]Oak Ridge National Laboratory, Oak Ridge, Tennessee, USA. [6]Section of Biomaterials, School of Dentistry, UCLA, Los Angeles, California, USA. [7]Division of Plastic and Reconstructive Surgery, Department of Surgery, David Geffen School of Medicine, UCLA, Los Angeles, California, USA.

NELL-1 is a secreted, osteogenic protein first discovered to control ossification of the cranial skeleton. Recently, NELL-1 has been implicated in bone maintenance. However, the cellular determinants of NELL-1's bone-forming effects are still unknown. Here, recombinant human NELL-1 (rhNELL-1) implantation was examined in a clinically relevant nonhuman primate lumbar spinal fusion model. Prolonged rhNELL-1 protein release was achieved using an apatite-coated β-tricalcium phosphate carrier, resulting in a local influx of stem cell antigen-1–positive (Sca-1$^+$) mesenchymal progenitor cells (MPCs), and complete osseous fusion across all samples (100% spinal fusion rate). Murine studies revealed that *Nell-1* haploinsufficiency results in marked reductions in the numbers of Sca-1$^+$CD45$^-$CD31$^-$ bone marrow MPCs associated with low bone mass. Conversely, rhNELL-1 systemic administration in mice showed a marked anabolic effect accompanied by increased numbers of Sca-1$^+$CD45$^-$CD31$^-$ bone marrow MPCs. Mechanistically, rhNELL-1 induces *Sca-1* transcription among MPCs, in a process requiring intact Wnt/β-catenin signaling. In summary, NELL-1 effectively induces bone formation across small and large animal models either via local implantation or intravenous delivery. NELL-1 induces an expansion of a bone marrow subset of MPCs with Sca-1 expression. These findings provide compelling justification for the clinical translation of a NELL-1–based therapy for local or systemic bone formation.

Authorship note: A.W. James and J. Shen contributed equally to this work.

Conflict of interest: X. Zhang, A.W. James, K. Ting, and C. Soo are inventors of NELL-1–related patents (patent numbers: US7052856, US7776361, US8207120, US7807787, US20030158602, US20060228392, US20110044956, WO 2001024821). X. Zhang, K. Ting, and C. Soo are founders and/or past board members of Bone Biologics Inc./Bone Biologic Corp., which sublicenses NELL-1 patents from the UC Regents, which also hold equity in the company.

Submitted: December 29, 2016
Accepted: May 5, 2017
Published: June 15, 2017

Reference information:
JCI Insight. 2017;2(12):e92573. https://doi.org/10.1172/jci.insight.92573.

Introduction

NELL-1 is a unique secreted protein of 810 amino acids first studied in the context of human craniofacial skeletal development, where NELL-1 was noted to be osteogenic and its overexpression associated with human craniosynostosis (CS) (1). Since that time, transgenic *Nell-1*–overexpressing mice have been observed to recapitulate a CS-like phenotype (2). Conversely, *Nell-1*–deficient mice (as developed by *N*-ethyl-*N*-nitrosourea–induced mutagenesis) exhibit cranial and vertebral bone defects with undermineralization (3). Recently, *Nell-1* haploinsufficiency has been observed to result in a low bone mineral density (BMD) phenotype, associated with hampered osteoblastic differentiation, reduced osteoblastic activity, and increased bone fragility (4). NELL-1 exerts regulatory effects on a broad array of mesenchymal cell types, including multipotent mesenchymal progenitor cells (MPCs) (4–7), committed preosteoblast cells (4, 8), odontoblasts (9), and chondrocytes (10–12). Mechanistically, NELL-1 binds to the cell surface heterodimer integrin α3β1 (13), resulting in several intracellular signaling changes that induce osteoblastogenic programming, including focal adhesion kinase (FAK) phosphorylation (14), increased mitogen-activated protein kinase (MAPK) signaling activity (15–17), and increased Wnt/β-catenin signaling activity (4, 18). Despite the well-demonstrated pro-osteogenic effects of NELL-1 (19–23), there has been little understanding of the cellular mediators of its effects, nor the role of NELL-1 in the maintenance or expansion of MPC pools.

Stem cell antigen-1 (Sca-1) is an 18-kDa glycosyl phosphatidylinositol–anchored cell surface protein of the Ly-6 family (24, 25). Most commonly studied as a marker of hematopoietic stem cells (HSCs) (25), Sca-1 is expressed on a wide variety of progenitor cell types, including a subset of bone marrow MPCs (24, 26). In addition, compact bone itself has been identified as a source of Sca-1$^+$ skeletal progenitor cells capable of trilineage differentiation potential (27). Sca-1$^+$ bone marrow progenitors have been shown to migrate to sites of bone turnover to aid in coupled bone remodeling (28). *Sca-1*$^{-/-}$ mice have multiple changes in hematopoietic cell content and function (29, 30), but also display a low-BMD phenotype that manifests with age (26). The skeletal phenotype of *Sca-1*$^{-/-}$ is related to a decrease in the self-renewal activity of bone marrow MPCs with age, but also defective osteoblastogenic differentiation and function, which is likely a secondary effect (26). The similarities in phenotype between *Nell-1*–deficient (4) and *Sca-1*$^{-/-}$ mice led us to examine the possible roles for NELL-1 signaling in regulation of the Sca-1$^+$ bone marrow MPC population.

Here, we identify across orthopedic models that NELL-1 expands the population of Sca-1–expressing bone marrow MPCs. First, a recombinant human NELL-1–based (rhNELL-1–based) bone graft substitute was applied in a nonhuman primate model of spinal fusion, leading to a recruitment of Sca-1$^+$ MPCs and complete spinal fusion in all samples. Second, systemic manipulation of Nell-1 signaling was achieved in mice, either via systemic infusion of rhNELL-1 protein, or 2 models of genetic loss. In each case, a substantial bone phenotype was correlated with corresponding changes in the Sca-1$^+$ MPC population abundance. In sum, the present study describes a potentially new role for Nell-1 signaling in the maintenance and expansion of Sca-1$^+$ mesenchymal progenitors, providing fresh insights into the cellular mediators of Nell-1 signaling in local and systemic bone formation.

Results

RhNELL-1 induces nonhuman primate lumbar spinal fusion accompanied by expansion of Sca-1$^+$ MPCs. Previous studies in rodent (20, 23, 31) and ovine models (22) have suggested that an rhNELL-1 protein–based bone graft substitute may be efficacious in promoting spinal fusion. In order to translate an rhNELL-1–based product to human patients, a nonhuman primate model of lumbar spine fusion was performed (Figure 1). Here, an intervertebral cage was packed using a demineralized bone matrix (DBX) alone (PBS control), or with 2 concentrations of rhNELL-1 protein (1.0 and 1.7 mg/ml). Prolonged release kinetics for rhNELL-1 were achieved via protein loading on surface-modified (apatite-coated) β-tricalcium phosphate (β-TCP) particles (Supplemental Figure 1; supplemental material available online with this article; https://doi.org/10.1172/jci.insight.92573DS1). Concentrations of rhNELL-1 were based on prior publications in ovine bone (22). Implant constituents are summarized in Table 1. A vertebral spacer packed with each treatment material was placed between either the L3/4 or L5/6 lumbar levels (see Figure 1A for schematic). Over the postoperative period, development of anti–human NELL-1 antibodies was ruled out, by assaying serum from all animals at postoperative weeks 2 and 12 (Table 2).

Radiographic assessments were performed using computed tomography (CT) of the entire instrumented segment (Supplemental Figure 2, shown in sagittal, coronal, and axial planes) and microCT for high resolution of the interbody space (Figure 1B, shown as a 3D reconstruction in the anterior-to-posterior perspective). A marked increase in radiodensity within the region of interest (ROI) was observed with rhNELL-1 application, especially at the 1.7 mg/ml dosage. Next, radiographic evidence of fusion was assessed based on our previously described methods (Table 3) (22). Control-treated and low-dose rhNELL-1–treated spinal fusion segments showed low radiographic evidence of fusion (25% fusion rate among each treatment group). In contrast, high-dose rhNELL-1 resulted in 100% radiographic evidence of fusion. Next, microCT-based quantification of bone within the interbody space was performed (Figure 1, C–G). In agreement with our qualitative findings, rhNELL-1 application led to an increase in BMD, percentage bone volume (BV/TV), and trabecular number (Tb.N) within the implant site. Conversely, rhNELL-1 treatment led to a reduction in trabecular spacing (Tb.Sp), while trabecular thickness (Tb.Th) remained unchanged in comparison with control. In order to test the biomechanical integrity of the intervertebral space, a computerized simulation of compression testing was performed. Here, a uniform 0.5 MPa force (used to simulate relaxed standing in human patients) was applied to random cubic volumes of interest (VOIs) within the spinal fusion segment, as examined by finite element analysis (FEA) (Figure 1, H and I). RhNELL-1 application led to a reduced predicted stress among cubic VOIs with the same applied force, shown by colored renderings (Figure 1H) and quantitative analysis of von Mises stress (Figure 1I).

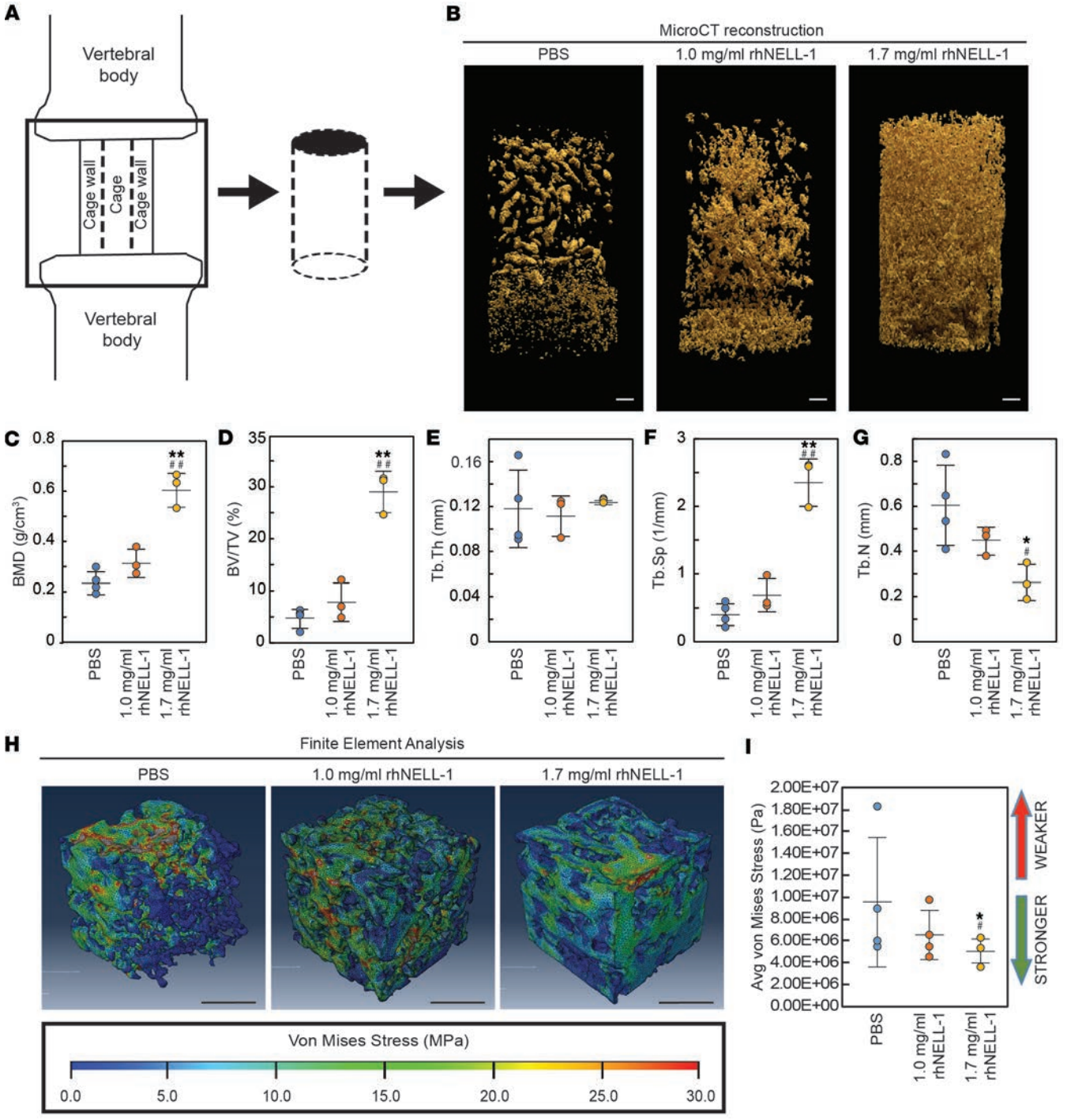

Figure 1. RhNELL-1 application in nonhuman primate lumbar spinal fusion: radiographic analysis. (**A**) Schematic diagram of nonhuman primate spinal fusion model. The rhNELL-1–based bone graft substitute was inserted within the spinal fusion cage. Contents of the spinal fusion cage are summarized in Table 1. Postoperative high-resolution microCT imaging was performed after 3 months. (**B**) Representative 3D anterior-posterior reconstructions of new bone within the interbody cage between lumbar vertebrae from PBS, 1.0 mg/ml rhNELL-1, and 1.7 mg/ml rhNELL-1 treatment groups at 3 postoperative months. (**C**–**G**) MicroCT analyses of the lumbar vertebral spinal fusion segment, including (**C**) bone mineral density (BMD), (**D**) bone volume/total volume (BV/TV), (**E**) trabecular bone thickness (Tb.Th), (**F**) trabecular spacing (Tb.Sp), and (**G**) trabecular number (Tb.N). (**H** and **I**) Computer-simulated biomechanical finite element analysis (FEA) and quantification of von Mises stress. Red color indicates areas of high calculated stress. $n = 4$ spinal fusion levels per treatment group, performed in single replicate. Values reported as mean ± SEM. $^{*}P < 0.05$, $^{**}P < 0.01$ in comparison with the PBS group using a 1-way ANOVA followed by a post-hoc Tukey's test. $^{\#}P < 0.05$, $^{\#\#}P < 0.01$ in comparison with the 1.0 mg/ml rhNELL-1 group. Scale bars: 1 mm.

Table 1. Contents of each implant across treatment groups in nonhuman primate spinal fusion model

Treatment group	*Apatite-coated TCP (mg)*	*RhNELL-1, total dose (mg)*	*DBX (cc)*
PBS	25	0	0.4
rhNELL-1 (1.0 mg/ml)	25	0.4	0.4
rhNELL-1 (1.7 mg/ml)	25	0.68	0.4

TCP, tricalcium phosphate; DBX, demineralized bone matrix.

Next, histologic and histomorphometric analysis of the spinal fusion segments was performed (Figure 2). Goldner's modified trichrome (GMT) and von Kossa-MacNeal's tetrachrome (VKMT) demonstrated increased bone formation within the intervertebral segment of rhNELL-1–treated samples, while control-treated samples showed predominantly fibrous tissue (Figure 2A). Histomorphometric quantification of serial VKMT-stained sections revealed a dose-dependent increase in bone formation with rhNELL-1 treatment (Figure 2B). Higher magnification images of H&E-stained sections revealed that the scaffold carrier (demineralized bone matrix) remained embedded in fibrous tissue and with minimal connections to adjacent demineralized bone fragments in the control-treated samples (Figure 2C). In contrast, rhNELL-1–treated samples showed a marked increase in new lamellar bone connections with the bone matrix fragments, as well as associated bone marrow elements and bone vascularization. Histomorphometric quantification of the fusion site vascularity likewise showed a marked increase among rhNELL-1–treated samples (Supplemental Figure 3).

Increasing stromal cellularity within the rhNELL-1–treatment spinal fusion samples led us to examine in more detail the cellular constituents within rhNELL-1–treated samples (Figure 3). Sca-1 is expressed in multiple progenitor cell types. Recognizing this, we examined Sca-1 expression in relation to both endothelial and hematopoietic cell markers. For this purpose, immunofluorescent detection of $CD31^+$ and $CD45^+$ cells was used to highlight endothelial and hematopoietic cell types, respectively (green images, Figure 3A). Immunofluorescent detection of Sca-1 expression was next performed (red images). Next, these 2 images were either overlaid on one another (appearing yellow, to identify Sca-1^+CD45/$CD31^+$ cells) or subtracted from one another to reveal Sca-$1^+CD45^-CD31^-$ stromal cells. No clear difference in total Sca-1^+ cells was observed across treatment groups (red images). Likewise, no change in total $CD45^+$ cells was seen across treatment groups. However, when $CD45^+$ and $CD31^+$ cells were removed, the remaining Sca-1^+CD45^- $CD31^-$ cells were significantly increased in number among rhNELL-1–treated samples. Semiquantitative histomorphometric analysis of relative staining area confirmed a marked increase in Sca-$1^+CD45^-CD31^-$ stromal cells with rhNELL-1 treatment (Figure 3B).

Nell-1 deficiency results in bone fragility with diminution of the Sca-1^+ MPC population. We previously examined the skeletal phenotype of *Nell-1*–haploinsufficient (*Nell-*$1^{+/6R}$) mice, showing that with skeletal aging a low-BMD, high-fragility bone phenotype emerges with reduced osteoblast numbers (4). Having observed a Sca-1^+ stromal cell expansion with local rhNELL-1 application, we next returned to our previously described *Nell-*$1^{+/6R}$ mouse and examined the Sca-1^+ stromal population within the bone marrow compartment (Figure 4). First, immunofluorescent localization of Sca-1^+ stromal cells was performed, using simultaneous detection of Sca-1, CD45, and CD31 (Figure 4, A and B). Representative images indicated that the majority of Sca-1^+ stromal cells are intramarrow stromal cells, with a few positive bone-lining cells (Figure 4B). The semiquantitative analysis revealed a marked depletion in the number of Sca-$1^+CD45^-CD31^-$ stromal cells within the bone marrow of *Nell-1*–deficient mice (Figure 4C). Next, and in order to further confirm these findings, flow cytometry for Sca-1^+ MPCs was performed (Figure 4, D and E). After selecting for the $CD45^-CD31^-$ population (P2), and positive selection for the progenitor cell markers CD105 and CD44 (P3), we next examined the expression of Sca-1 (P4) (Figure 4D). Findings by flow cytometry demonstrated that wild-type mice had a gradual reduction in Sca-1^+ MPCs with age (as defined by the fraction of Sca-$1^+CD45^-CD31^-CD105^+CD44^+$ bone marrow cells, Figure 4E). Across all time points, *Nell-*$1^{+/6R}$ mice showed a marked reduction in Sca-1^+ MPCs, which temporally preceded the development of the low-BMD phenotype (4). We next confirmed these findings using a second *Nell-1*–deficient mouse, this one generated using the Cre-LoxP system (Figure 4F). Here, *Nell-*$1^{fl/fl}$ mice were crossed with CMV-Cre mice to result in constitutive loss of *Nell-1* expression (*Nell-*$1^{fl/fl}$;CMV-Cre). Like the *Nell-*$1^{+/6R}$ mice, *Nell-*$1^{fl/fl}$;CMV-Cre animals showed a marked reduction in Sca-1^+ MPCs within the bone marrow compartment.

Table 2. Anti–NELL-1 IgG serum levels during the course of spinal fusion in nonhuman primates

Treatment Groups	Preoperative (mean OD ± SD)[A]	2 Postoperative weeks (mean OD ± SD)	12 Postoperative weeks (mean OD ± SD)
PBS	0.0695 ± 0.0033	0.0619 ± 0.0049	0.0644 ± 0.0024
rhNELL-1 (1.0 mg/ml)	0.0573 ± 0.0047	0.0611 ± 0.0064	0.0570 ± 0.0021
rhNELL-1 (1.7 mg/ml)	0.0548 ± 0.0029	0.0570 ± 0.0057	0.0539 ± 0.0022

[A]OD for blank control (mean OD ± SD) = 0.0222 ± 0.0020; OD for negative control (mean OD ± SD) = 0.0647 ± 0.0072; OD for positive control (mean OD ± SD) = 1.0831 ± 0.0430.

Systemic rhNELL-1 demonstrates anabolic effects with Sca-1$^+$ MPC expansion. Recently, we reported that intravenous administration of rhNELL-1 protein results in a marked anabolic effect in mice, and reverses the effects of ovariectomy-induced loss of BMD (4). Next, we replicated this protocol in nonovariectomized animals (Figure 5). RhNELL-1 or PBS control was administered by tail vein injection every 48 hours, as per our previous treatment regimen (4). Trabecular bone of the distal femur was examined after 4 weeks of treatment. MicroCT analysis showed a qualitative increase in trabecular bone in the distal femoral metaphysis with rhNELL-1 treatment (Figure 5A). Quantitative analysis of the trabecular bone was next performed by microCT (Figure 5, B–G). In agreement with our prior studies (4), results showed that rhNELL-1–treated samples had increased trabecular BMD, increased BV, and fractional BV/TV (Figure 5, B–D). Trabecular indices were also significantly changed, including increased Tb.Th, and a trend toward increased Tb.N (Figure 5, E–G). Dynamic histomorphometry within the trabecular bone of the distal metaphysis was next performed (Figure 5, H and I). Results showed a significant increase in mineral apposition rate (MAR) and bone formation rate among rhNELL-1–treated samples. Finally, computer-simulated (FEA) biomechanical analysis was performed of the femoral midshaft (Figure 5, J and K). With a uniform compressive force, significantly reduced von Mises stress was observed among rhNELL-1–treated samples (Figure 5K).

We next inquired as to whether rhNELL-1 intravenous administration correlated with any differences in the Sca-1$^+$ MPC population within the bone marrow milieu. Immunofluorescent costaining for Sca-1, CD31, and CD45 was again performed (Figure 6). Although no difference in the total Sca-1 population was identified, a significant increase in the Sca-1$^+$CD45$^-$CD31$^-$ stromal population was appreciated (far right column, Figure 6A). Semiquantitative analysis of immunofluorescent staining confirmed a significant increase in the Sca-1$^+$CD45$^-$CD31$^-$ stromal population (Figure 6B). Among bone-lining Sca-1$^+$ cells, a large proportion of cells colocalized with the osteoblast marker osteocalcin (Ocn) (Supplemental Figure 4). To further confirm, flow cytometry of mouse bone marrow with or without rhNELL-1 intravenous treatment was performed (Figure 6C). In agreement with immunohistochemical findings, we again observed a significant increase in the Sca-1$^+$CD105$^+$CD44$^+$CD45$^-$CD31$^-$ cell population among rhNELL-1–treated samples (Figure 6C).

NELL-1 regulates the transcription of Sca-1, which requires intact Wnt signaling activity. NELL-1–mediated regulation of the Sca-1 cell population could be exerted on many levels, including expansion of an existing Sca-1$^+$ population, or changing the Sca-1 expression within an existing Sca-1$^-$ cell population. To begin to dissect out this mechanism, the mouse multipotent cell line M2-10B4 was cultured in the presence or absence of rhNELL-1 (Figure 6D). Remarkably, a significant increase in *Sca-1* transcripts was seen when cells were placed either in growth medium (Figure 6D) or osteogenic differentiation medium (not shown). We previously demonstrated that the pro-osteogenic effects of rhNELL-1 require intact Wnt/β-catenin signaling (4). Cotreatment with the extracellular Wnt antagonist DKK1 was next undertaken. While DKK1 alone showed no effect on *Sca-1* transcript abundance, DKK1 completely abrogated the rhNELL-1–mediated increase in *Sca-1* transcripts. Thus, NELL-1–mediated transcriptional increase in *Sca-1* requires intact Wnt/β-catenin signaling.

Discussion

In summary, we report that NELL-1 induces clinically significant bone formation when applied on either local or systemic levels, and that this is accompanied by an expansion of Sca-1$^+$ mesenchymal progenitor/stromal cells. NELL-1 regulates *Sca-1* transcript abundance, in a mechanism that requires intact Wnt/β-catenin signaling. Finally, a NELL-1–based bone graft substitute product results in successful lumbar spinal fusion in a clinically relevant nonhuman primate model.

Table 3. Nonhuman primate spinal fusion rates

Treatment Groups	Percentage fused (%)	Fraction fused (n/4)
PBS	25	1/4
rhNELL-1 (1.0 mg/ml)	25	1/4
rhNELL-1 (1.7 mg/ml)	100	4/4

Fusion rate of lumbar vertebral segment with PBS, 1.0 mg/ml rhNELL-1, or 1.7 mg/ml rhNELL-1 treatment. Fusion rate was determined after 3 months, using CT images with 50% or greater area of contiguous bridging bone within the implant site. *n* = 4 spinal fusion levels per treatment group, performed in single replicate.

Although we observed a clear linkage between Nell-1 signaling and Sca-1$^+$ MPC numbers across multiple orthopedic models, the exact nature of this link remains only partially elucidated. First, the exact identity of bone marrow–resident Sca-1$^+$ MPCs is still poorly understood. In particular, it is unclear if the Sca-1$^+$CD45$^-$CD31$^-$ stromal population are bona fide MPCs, their committed osteoblastic progeny, or a combination of the 2. It is worthwhile to note that the same NELL-1–mediated increase in Sca-1$^+$ cells was observed by multiple analytic methods, including immunofluorescent localization and flow cytometry. In the case of immunofluorescent localization, Sca-1$^+$ progenitors were examined as a fraction of the nonhematopoietic, nonendothelial population. In the case of flow cytometry, this was extended to examine Sca-1$^+$ progenitors as a fraction of the CD105$^+$CD44$^+$ progenitor cell population. In future studies, further MPC markers may be used for better delineation of the Sca-1$^+$ progenitor subset expanded by NELL-1. Clues from *Sca-1*–null animals suggest that combinatorial influence on bona fide MPCs and more committed progeny may be more likely, as global loss of Sca-1 results in a wide spectrum of cellular changes including a reduction in uncommitted stromal progenitors, a reduction in more committed osteoprogenitor cells, and clear reduction in mature osteoblastic activity (26).

In addition, the nature of the link between NELL-1 and Sca-1$^+$ MPCs is also not completely defined. We initially hypothesized that local NELL-1 implantation/administration may result in recruitment of MPCs to sites of bone injury, similar to the described function of latent TGF-β released after bone injury (28). Nevertheless, our broader findings of Sca-1$^+$ MPC population changes with systemic augmentation or deficiency in Nell-1 suggest more than a promigratory effect. Perhaps a mitogenic effect underlies these changes in Sca-1$^+$ MPC numbers. Previously we observed that NELL-1 has context-specific mitogenic effects, and particularly that the short isoform of *Nell-1* appears to have greater pro-proliferative effects on MPCs than the more common long isoform (existing as 570 and 810 amino acids, respectively) (7). Nevertheless, the mitogenic effects of NELL-1 protein are modest and it is unclear if this alone underlies the significant changes in Sca-1$^+$ cell numbers observed here. Finally, we observed that NELL-1 controls *Sca-1* gene expression under isolated in vitro conditions in a bone marrow stromal cell line in a process that is dependent on intact canonical Wnt signaling. This brings up the interesting possibility that NELL-1 induces a shift in phenotype among bone marrow stromal cells, with a resulting overall change to a larger Sca-1$^+$ MPC subset.

Overall, NELL-1 possesses several practical and theoretical benefits as a potential anabolic therapy for bone. NELL-1 has documented tumor-suppression properties and its expression is lost in several carcinomas (32, 33). Recently, we documented high expression of NELL-1 among several bone- and cartilage-forming tumors, but its expression does not correlate with benign and malignant tumor types (34, 35). Finally, NELL-1 has an excellent safety profile. Mice with constitutive *Nell-1* overexpression have a normal lifespan, and are without abnormalities excepting the skeleton (2). Similarly, 5-day intravenous rhNELL-1 toxicity testing in mice found no gross pathologic, histopathologic, or biochemical abnormalities (4). Likewise, no adverse effects were observed in the current nonhuman primate spinal fusion model. However, it is important to note that Nell-1 signaling has known functions in an array of developmental processes, including neurogenesis (36), chondrogenesis (11), and vasculogenesis (37). With this in mind, a more thorough study of these off-bone effects of NELL-1 must be instituted before consideration of rhNELL-1 as a clinical therapy.

In summary, we identify across orthopedic models that NELL-1 expands the population of Sca-1–expressing bone marrow MPCs. These observations ranged from a clinically relevant nonhuman primate model of spine fusion, to intravenous treatment in the mouse. In each circumstance, a clear-cut link between NELL-1 treatment and Sca-1$^+$ MPC numbers was seen. In sum, the present study describes a potentially new role for NELL-1 in the maintenance or expansion of Sca-1$^+$ mesenchymal progenitors, providing fresh insights into the cellular mediators of NELL-1 in local and systemic bone formation.

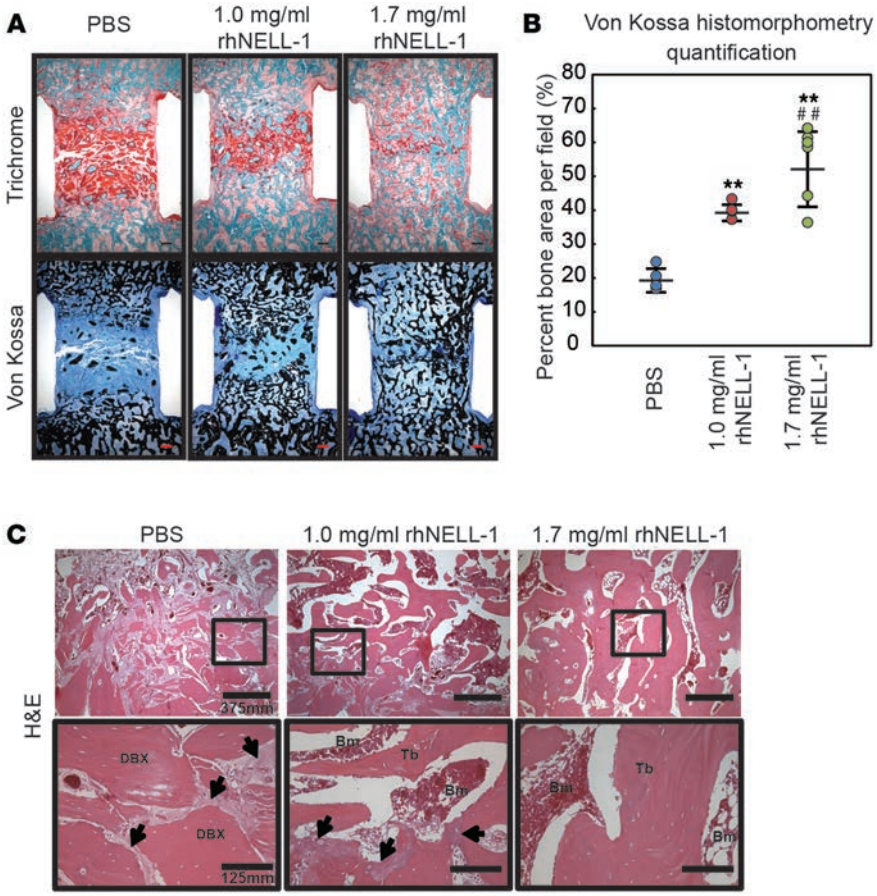

Figure 2. RhNELL-1 application in nonhuman primate lumbar spinal fusion: histologic analysis. (**A**) Goldner's modified trichrome (GMT) and von Kossa-MacNeal's tetrachrome (VKMT) staining of nonhuman lumbar vertebral spinal fusion segment from PBS, 1.0 mg/ml rhNELL-1, and 1.7 mg/ml rhNELL-1 treatment groups. Images are shown in coronal cross section and include the centrally located spinal fusion segment, with each vertebral body on the lower and upper aspects of the image. Scale bars: 1 mm. (**B**) Quantification of VKMT histomorphometric analysis. Three random fields within the spinal fusion segment were analyzed per slide, with 2–3 slides per sample. (**C**) Representative H&E staining of lumbar vertebral spinal fusion segment from PBS, 1.0 mg/ml rhNELL-1, and 1.7 mg/ml rhNELL-1 treatment groups. $n = 4$ spinal fusion levels per treatment group, performed in single replicate. $^{**}P < 0.01$ compared with the PBS group. $^{\#\#}P < 0.01$ compared with the 1.0 mg/ml rhNELL-1 group, analyzed using a 1-way ANOVA followed by a post-hoc Tukey's test. Bm, Bone marrow; DBX, demineralized bone matrix putty; Tb, trabecular bone.

Methods

Animal care. Matings were done overnight and females were examined for the presence of vaginal plugs at 0.5 days postcoitum. Animal groups were of mixed gender unless otherwise stated. C57BL/6 mice were obtained from Charles River Laboratories.

Heterozygote carriers of the *Nell-1*$^{+/6R}$ gene were provided by the Mammalian Genetic Research Facility at Oak Ridge National Laboratory and were transferred with permission of the Chancellor's Animal Research Committee (4). The *Nell-1*$^{6R/6R}$ mouse genotypes were identified from DNA extracted from clipped tails of mutant and wild-type mice. The extracted DNA was amplified using microsatellite primers: D7Mit 315-L, TGATAACAAAACAGTCAGTATGAAGC; D7Mit 315, RCTGATCCATCTGTATGATGTTACTTG. Mixed-gender animals were used unless otherwise stated.

Nell-1$^{fl/fl}$ mice were generated by flanking the exon 1–containing ATG site with loxP, and then removing the FRT-flanked Neo cassette with FLPo-deleter mice in the C57BL/6 background (obtained from the Jackson Laboratory, B6.Cg-Tg(Pgk1-flpo)10Sykr/J). CMV-Cre transgenic mice were purchased from The Jackson Laboratory and used to obtain *Nell-1*$^{fl/fl}$;CMV-Cre mice. Genotyping and gene expression of *Nell-1* were performed by PCR and quantitative reverse transcription PCR (qRT-PCR), respectively, to confirm the knockout before isolating bone marrow MPCs for flow cytometric

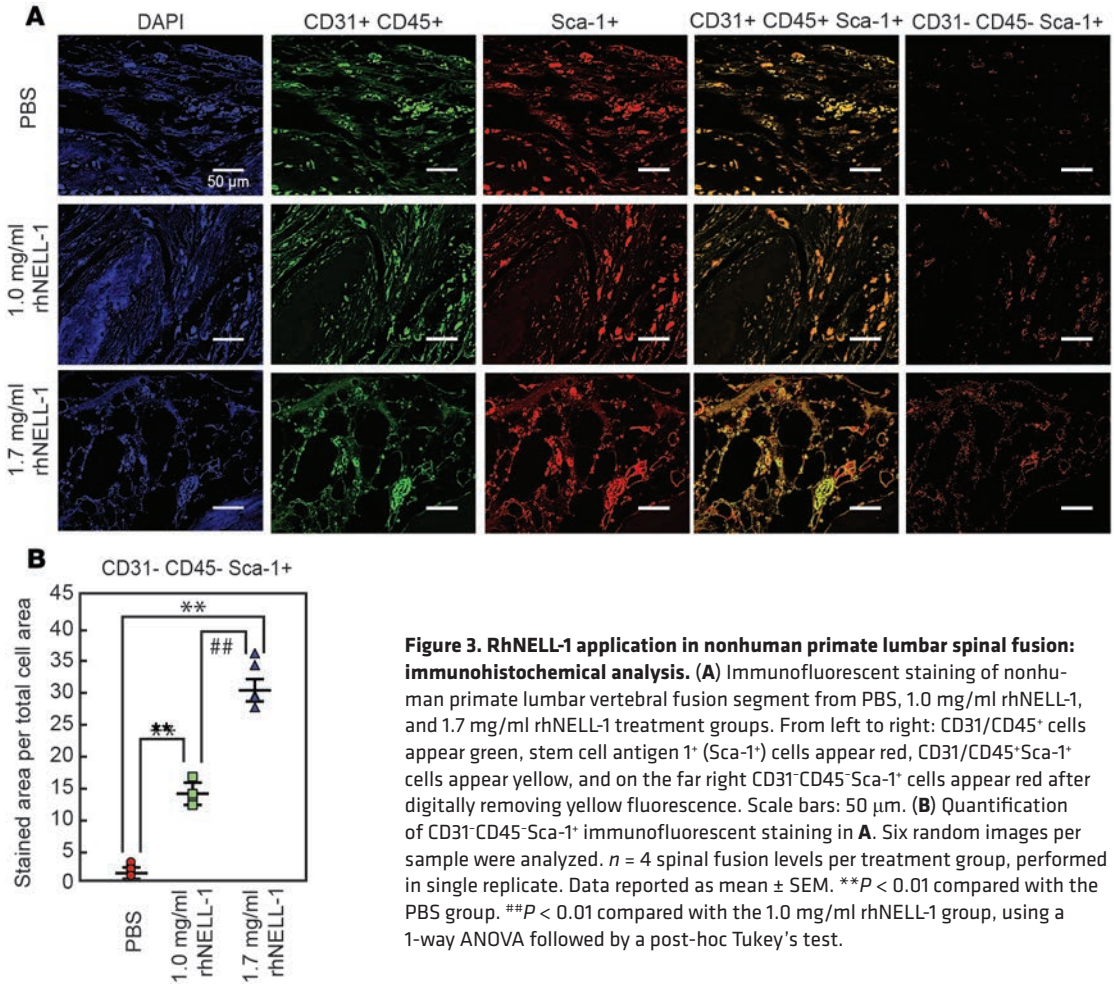

Figure 3. RhNELL-1 application in nonhuman primate lumbar spinal fusion: immunohistochemical analysis. (**A**) Immunofluorescent staining of nonhuman primate lumbar vertebral fusion segment from PBS, 1.0 mg/ml rhNELL-1, and 1.7 mg/ml rhNELL-1 treatment groups. From left to right: CD31/CD45$^+$ cells appear green, stem cell antigen 1$^+$ (Sca-1$^+$) cells appear red, CD31/CD45$^+$Sca-1$^+$ cells appear yellow, and on the far right CD31$^-$CD45$^-$Sca-1$^+$ cells appear red after digitally removing yellow fluorescence. Scale bars: 50 μm. (**B**) Quantification of CD31$^-$CD45$^-$Sca-1$^+$ immunofluorescent staining in **A**. Six random images per sample were analyzed. n = 4 spinal fusion levels per treatment group, performed in single replicate. Data reported as mean ± SEM. $^{**}P < 0.01$ compared with the PBS group. $^{\#\#}P < 0.01$ compared with the 1.0 mg/ml rhNELL-1 group, using a 1-way ANOVA followed by a post-hoc Tukey's test.

analysis. Mixed-gender animals were used unless otherwise stated. The Cre-negative littermates were used as wild-type control. All mice were housed in the light- and temperature-controlled UCLA vivarium, and provided water and feed ad libitum.

All nonhuman primate care and surgical procedures was approved by the Institutional Committee on Laboratory Animal Use (IULAC) of Shandong University. Male, 5- to 7-year-old Rhesus macaques (*Macaca mulatta*), each weighing an average of 5 to 8 kg, were used for intervertebral spinal fusion surgery. Monkeys were euthanized by barbiturate overdose at 3 months postoperatively. Whenever possible, animals were randomized with even distribution across treatment groups.

For all in vivo studies, all samples were included in subsequent analyses. No exclusion criteria were used.

Mouse rhNELL-1 intravenous injection. RhNELL-1 delivery by intravenous injection was instituted by lateral tail vein injection using a 25-gauge needle, as previously described (4). Animals were assigned to treatment groups by simple randomization. Drug administrators were completely blinded as to treatment groups. The dosage of rhNELL-1 (1.25 mg/kg) was obtained as per prior studies (4). PBS served as a vehicle control. Each injection consisted of a total 0.1 ml solution, and injection was performed every 48 hours for the study period. Animals were sacrificed 4 weeks after initiating treatment.

Murine microCT and FEA. For rhNELL-1 treatment studies, high-resolution, postmortem microCT scanning and analysis were performed on the distal femoral metaphysis of murine samples. Samples were harvested, formalin fixed and imaged using high-resolution microCT (Skyscan 1172F) at an image resolution of 17.8 to 28.2 μm and analyzed using DataViewer, Recon, CTAn, and CTVol software provided by the manufacturer. Trabecular analysis was performed on the distal femoral metaphysis, for which ROIs were drawn to exclude cortical bone. Reconstructions were performed using Osirix software, using coronal cross-sectional images with a 0.25-μm width. All quantitative and structural morphometric data use nomenclature described by the American Society for Bone and Mineral Research (ASBMR) Nomenclature Committee (38). MicroCT indices were

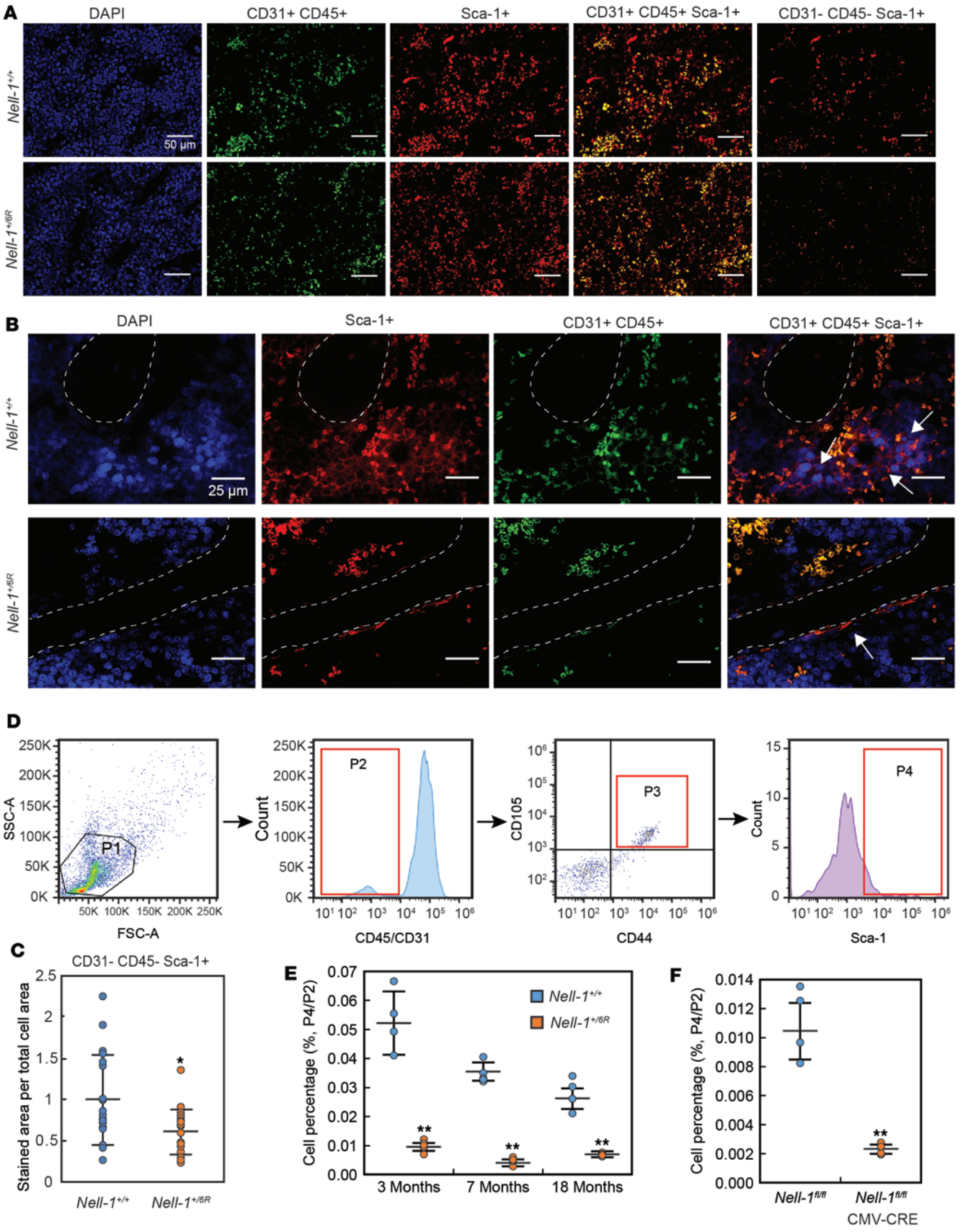
A
DAPI
CD31+ CD45+
Sca-1+
CD31+ CD45+ Sca-1+
CD31- CD45- Sca-1+
Nell-1+/+
Nell-1+/6R
50 μm
B
DAPI
Sca-1+
CD31+ CD45+
CD31+ CD45+ Sca-1+
25 μm
D
SSC-A
FSC-A
P1
Count
CD45/CD31
P2
CD105
CD44
P3
Sca-1
P4
C
CD31- CD45- Sca-1+
Stained area per total cell area
E
Cell percentage (%, P4/P2)
3 Months
7 Months
18 Months
F
Nell-1fl/fl
CMV-CRE

Figure 4. *Nell-1* deficiency in mice results in reduced Sca-1⁺ progenitor cell numbers. (**A**) Immunofluorescent staining of CD31⁻CD45⁻Sca-1⁺ cells in mouse bone marrow of WT and *Nell-1*$^{+/6R}$ mice, analyzed at 3 months of age. From left to right: CD31/CD45⁺ cells appear green, stem cell antigen 1⁺ (Sca-1⁺) cells appear red, CD31/CD45⁺Sca-1⁺ cells appear yellow, and on the far right CD31⁻CD45⁻Sca-1⁺ cells appear red after digitally removing all yellow fluorescence. Scale bars: 50 μm. (**B**) At high magnification, the localization and type of CD31⁻CD45⁻Sca-1⁺ cells (arrows) was revealed, with the majority of cells residing in an intramarrow location, with scattered bone lining cells stained. Dashed white lines indicate margins of trabecular bone. DAPI nuclear counterstain appears blue. Scale bars: 25 μm. (**C**) Semiquantification of staining presented in **A**. Six random fields were analyzed per slide with 3 slides analyzed per sample. (**D**) Representative flow cytometry methods for Sca-1⁺ cell quantification. After selecting for the CD31⁻CD45⁻ population (P2), and positive selection for the mesenchymal progenitor cell (MPC) markers CD105 and CD44 (P3), the subpopulation of Sca-1⁺ (P4) was then selected. (**E**) Flow cytometric analysis of CD31⁻CD45⁻CD105⁺CD44⁺Sca-1⁺ population in mouse bone marrow of WT and *Nell-1*$^{+/6R}$ mice, analyzed at 3, 7, and 18 months of age. Percentage of cells expressed as CD31⁻CD45⁻CD105⁺CD44⁺Sca-1⁺ cells over total CD31⁻CD45⁻ cells. (**F**) Flow cytometric analysis of the CD31⁻CD45⁻CD105⁺CD44⁺Sca-1⁺ population in mouse bone marrow of CMV-Cre⁺*Nell-1*$^{+/+}$ and CMV-Cre⁺*Nell-1*$^{fl/fl}$ mice at 3 months of age. Percentage of cells expressed as CD31⁻CD45⁻CD105⁺CD44⁺Sca-1⁺ cells over total CD31⁻CD45⁻ cells. Data reported as mean ± SEM. $^{*}P < 0.05$ and $^{**}P < 0.01$ compared with respective controls. Analyzed using a 2-tailed Student's *t* test (**C** and **F**) or a 1-way ANOVA followed by a post-hoc Tukey's test to compare between 2 groups (**E**).

compared to published norms to ensure accuracy of analysis and reporting (39–41). Whenever possible, all radiographic studies were performed and quantified in a blinded fashion.

For biomechanical testing, FEA was performed using microCT images converted to DICOM files using SKyScan Dicom Converter software (DicomCT application, Skyscan 1172F). Tetrahedral 3D mesh models were created using a VOI of the mid femoral diaphysis using ScanIP software (Simpleware Limited). A constant thickness of 0.54 mm was used for each VOI. FEAs were performed using ABAQUS software version 6.12 (Dassault Systèmes) with boundary conditions set as encastre, constrained in all directions. Next, we applied a uniform compressive pressure of 0.5 MPa on the superior surface of the VOI. The von Mises stress experienced and total strain energy of the samples were analyzed. $n = 8$ mice per genotype for FEAs.

Murine histologic analyses. For histology, all tissues were fixed in 10% PBS-buffered formalin. Mouse samples were decalcified in 19% EDTA, and embedded in paraffin. Five-micron-thick sections were made and stained with H&E (4). Histological specimens were analyzed using an Olympus BX51 microscope and images acquired using MicroFire digital camera with Picture Frame software (Optronics).

Immunofluorescent staining was performed for Alexa 488–conjugated CD31 (102414, Biolegend), Alexa 488–conjugated CD45 (103122, Biolegend), rat anti–mouse Sca-1 (51317, Abcam), and rabbit anti–mouse Ocn (sc-30045, Santa Cruz Biotechnology). Initially, sections were deparaffinized, dehydrated, rinsed, and incubated with 3% H_2O_2 for 20 minutes and then blocked with 0.1% BSA in PBS for 1 hour. All 3 primary antibodies were added to each section at a dilution of 1:200 and incubated at 37°C for 1 hour and at 4°C overnight. Trypsin-induced epitope retrieval was performed for 20 minutes at room temperature, using the Digest-All 2 system (00-3008, Invitrogen). The ABC complex (Vector Laboratories) was applied to the sections after the incubation with a biotinylated anti-rat secondary antibody (Dako) or donkey anti–rabbit IgG-FITC (sc-2090, Santa Cruz Biotechnology). Positive immunoreactivity was detected following incubation and development with Texas Red Streptavidin (SA-5006, Vector Laboratories) at a dilution of 1:50. Slides were counterstained and mounted with Vectashield mounting medium for fluorescence with DAPI (H-1200, Vector Laboratories). Images (original magnification, ×200; 5–6 random fields per slide) were analyzed by semiquantitative analysis using the magic wand tool in Adobe Photoshop to quantify the relative stain intensity across groups. The relative stain intensity was determined by total area of red fluorescence (representing Sca-1⁺CD45⁻CD31⁻ cells) with a tolerance level of 30, adjusted for the total blue fluorescence (representing the nuclear counterstain). Areas of overlapping green and red fluorescence (Sca1⁺CD45/CD31⁺) appeared as yellow, and were thus not included in the quantification. All image acquisition and analysis was performed in a blinded fashion.

For bone fluorescence-labeling studies, mice were injected intraperitoneally with calcein (20 mg/kg) and alizarin red complexion (50 mg/kg) at 9 days and 2 days before sacrifice, respectively. Femoral bones were dissected, fixed in 70% ethanol, dehydrated, and embedded undecalcified in methyl methacrylate. Coronal sections of the distal femur at 5 μm thickness were analyzed using the OsteoMeasure morphometry system (Osteometrics). For dynamic histomorphometry, the mineral apposition rate (MAR, μm/d) — the distance between the midpoints of the 2 labels divided by the time between the midpoints of the interval — was measured in unstained sections under UV light and used to calculate bone formation rate with a bone surface referent (BFR/BS, $\mu m^3/\mu m^2/y$). Bone formation rate per bone surface (BFR/BS) is the volume of mineralized bone formed per unit time and per unit bone surface. All image acquisition and analysis was performed in a blinded fashion.

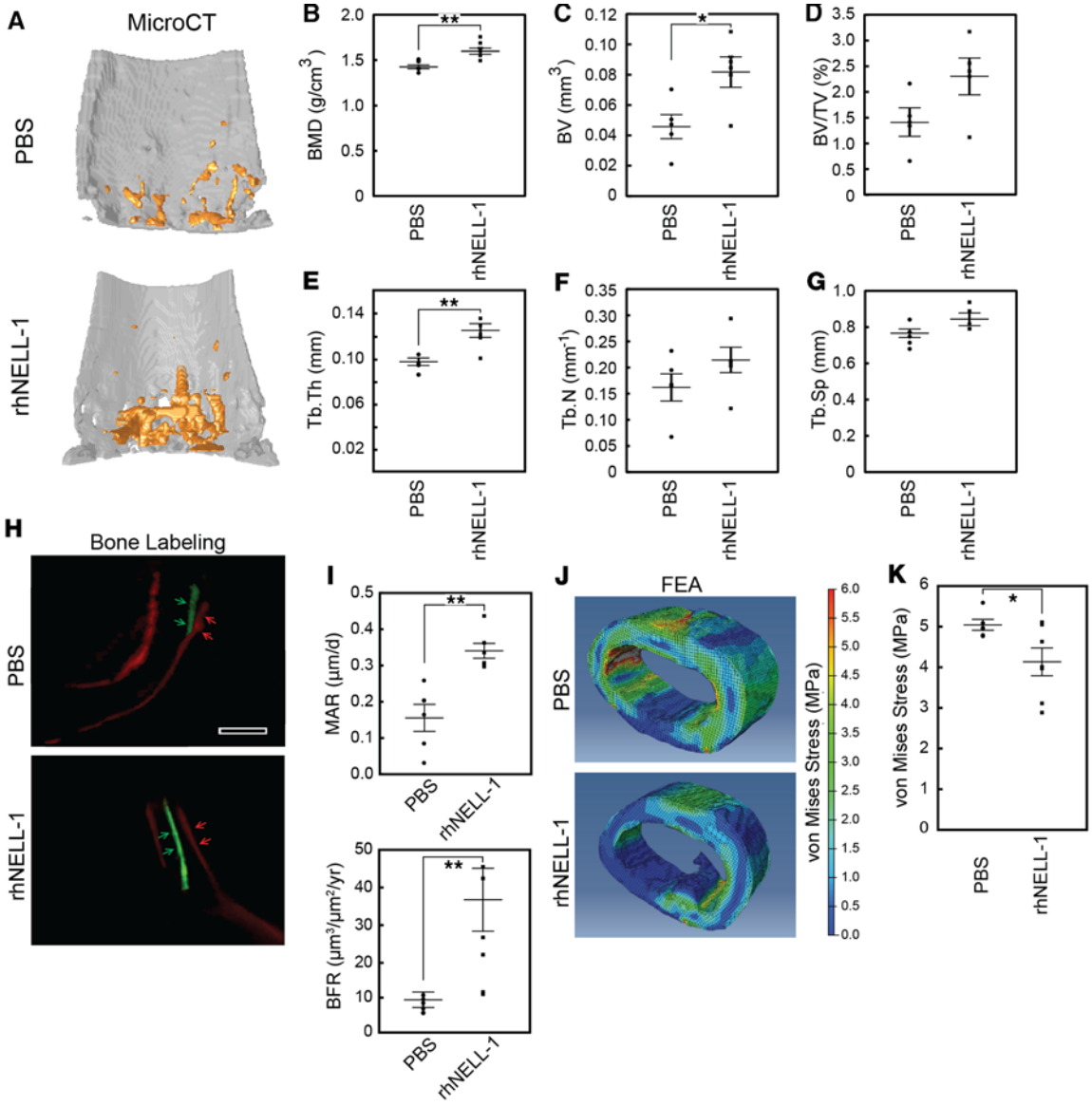

Figure 5. RhNELL-1 systemic injection in mouse: radiographic analysis. (**A**) MicroCT analyses of mice injected with PBS or rhNELL-1 (1.25 mg/kg). (**B**–**G**) Absolute change in bone mineral density (BMD), bone volume (BV), bone volume/tissue volume (BV/TV), trabecular thickness (Tb.Th), trabecular number (Tb.N), and trabecular spacing (Tb.Sp) among control- and rhNELL-1–treated distal femoral metaphysis by microCT quantification. (**H** and **I**) Calcein/alizarin red complex on bone labeling and quantification of mineral apposition rate (MAR) and bone formation rate (BFR). Red and green arrows highlight the space between fluorochrome labels. Scale bar: 25 μm. (**J** and **K**) Finite element analysis (FEA) and quantification of von Mises stress within the femoral midshaft. Data reported as mean ± SEM. n = 5–6 samples per group, single replicate. $^{*}P < 0.05$, $^{**}P < 0.01$ compared with the PBS group, using a 2-tailed Student's t test.

Flow cytometric analysis of murine bone marrow. Whole bone marrow was flushed from the mouse bilateral femurs. Red blood cells were lysed using RBC lysis buffer (420301, Biolegend). Marrow cells (1×10^6) in suspension were stained with preconjugated CD45-FITC (103122, Biolegend), CD31-FITC (102414, Biolegend), CD44-APC-Cy7 (560568, BD Biosciences), CD105-PE (562759, BD Biosciences), and Sca-1-PE-Cy7 (558162, BD Biosciences) antibodies in 100 μl (0.25 μg per antibody) for 20 minutes on ice. Nonspecific binding was blocked by incubation in FACS buffer (Life Technologies) containing 0.5% BSA and 40 nM EDTA (Sigma-Aldrich). Following incubation, the unbound antibodies were removed using a 1-ml wash of FACS buffer 3 times. Analyses were performed on a BD LSR II flow cytometer (BD Biosciences). The data were analyzed with FlowJo software. Experiments were performed in triplicate unless otherwise noted.

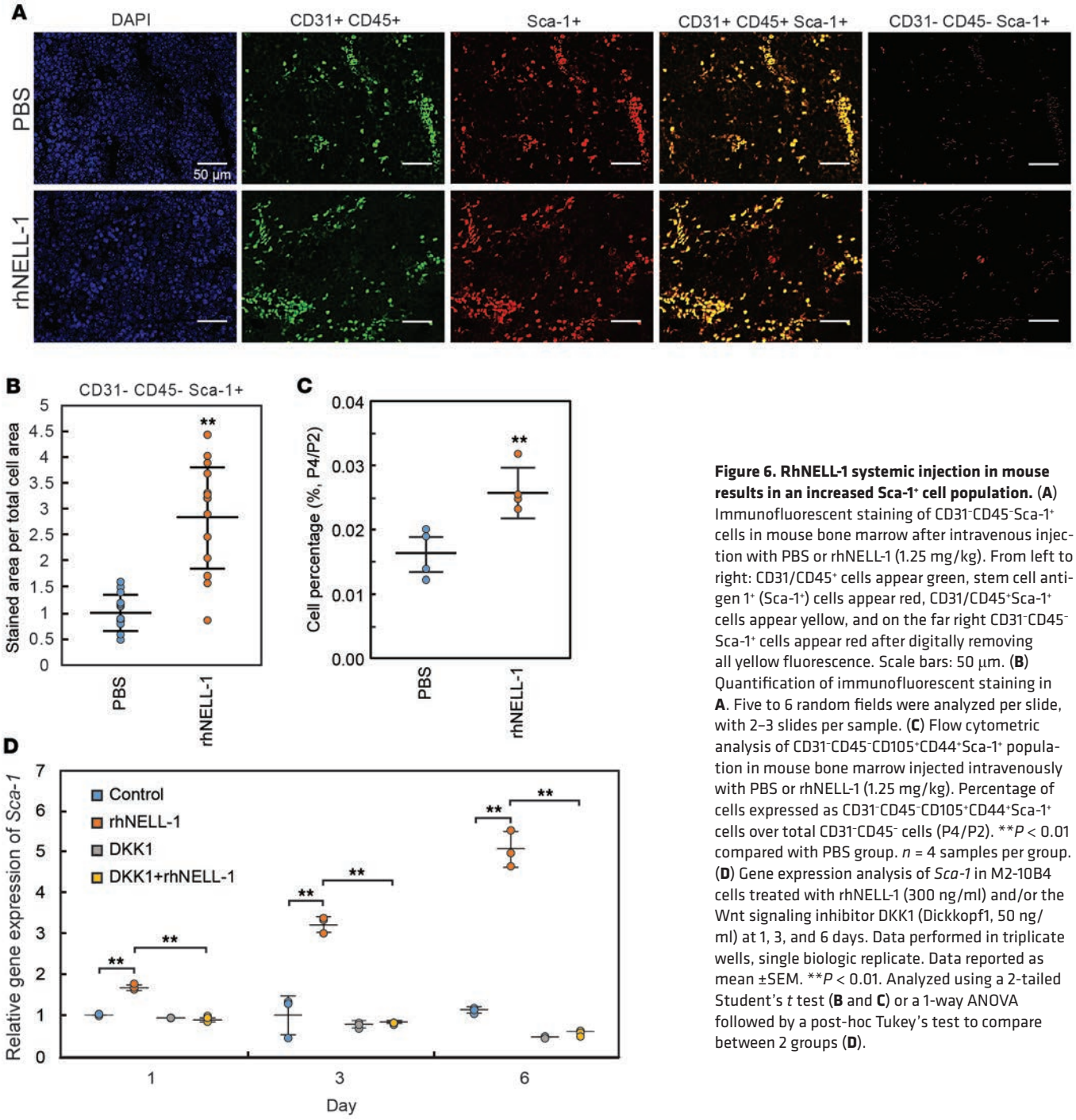

Figure 6. RhNELL-1 systemic injection in mouse results in an increased Sca-1⁺ cell population. (**A**) Immunofluorescent staining of CD31⁻CD45⁻Sca-1⁺ cells in mouse bone marrow after intravenous injection with PBS or rhNELL-1 (1.25 mg/kg). From left to right: CD31/CD45⁺ cells appear green, stem cell antigen 1⁺ (Sca-1⁺) cells appear red, CD31/CD45⁺Sca-1⁺ cells appear yellow, and on the far right CD31⁻CD45⁻Sca-1⁺ cells appear red after digitally removing all yellow fluorescence. Scale bars: 50 μm. (**B**) Quantification of immunofluorescent staining in **A**. Five to 6 random fields were analyzed per slide, with 2–3 slides per sample. (**C**) Flow cytometric analysis of CD31⁻CD45⁻CD105⁺CD44⁺Sca-1⁺ population in mouse bone marrow injected intravenously with PBS or rhNELL-1 (1.25 mg/kg). Percentage of cells expressed as CD31⁻CD45⁻CD105⁺CD44⁺Sca-1⁺ cells over total CD31⁻CD45⁻ cells (P4/P2). $^{**}P < 0.01$ compared with PBS group. $n = 4$ samples per group. (**D**) Gene expression analysis of *Sca-1* in M2-10B4 cells treated with rhNELL-1 (300 ng/ml) and/or the Wnt signaling inhibitor DKK1 (Dickkopf1, 50 ng/ml) at 1, 3, and 6 days. Data performed in triplicate wells, single biologic replicate. Data reported as mean ±SEM. $^{**}P < 0.01$. Analyzed using a 2-tailed Student's *t* test (**B** and **C**) or a 1-way ANOVA followed by a post-hoc Tukey's test to compare between 2 groups (**D**).

Cell culture and gene expression analyses. The M2-10B4 stromal cell line was cultured in DMEM + 10% FBS (ATCC, CRL-1972, lot 58696031) within 6 months of mycoplasma contamination testing. Cells were seeded on 6-well plates at a density of 5×10^4/well, and cells were treated with rhNELL-1 (300 ng/ml) and/or DKK-1 protein (50 ng/ml) with medium changed every day. Gene expression was analyzed at the indicated time point by qRT-PCR. RNA was extracted using TRIzol (Life Technologies; according to the manufacturer's instructions) and the first strand complementary DNA was synthesized from 1 μg of total RNA using a SuperScript III First-Strand Synthesis System (Fermentas). qRT-PCR was performed using a 7300 Real-Time PCR System machine with SYBR Green Real-Time PCR Master Mixes (both Life Technologies). The targeted primer sequences for Sca1 are 5′-CGAGGGAGGGAGCTGTGAGGTT-3′ and antisense, 5′-GAGGGCAGATGGGTAAGCAAA-

GAT-3′; and β-actin, 5′-GAGCAAGAGAGGTATCCTGAC-3′ and antisense, 5′-TTCATGGATGC-CACAGGATTC-3′. The data were normalized to the geometric means of the reference genes β-actin and analyzed using a comparative Ct method where ΔCt is the difference between the Ct values of the target and the geometric mean of the reference genes.

Nonhuman primate spine fusion preparation and surgery. Six nonhuman primates were used for intervertebral spinal fusion surgery, with methods adopted from our prior reports in ovine spinal fusion (22). As in prior reports, a 2-level spinal fusion was performed (on lumbar levels L3/4 and L5/6), yielding 2 data points per animal. The scaffold material consists of a DBX putty, provided by the Musculoskeletal Transplant Foundation. DBX putty consists of morselized Rhesus macaque cortical-cancellous demineralized bone chips with sodium hyaluronate, and was chosen for its proven osteoinductive characteristics and clinical translational potential (human DBX is already 510(k) approved). For extended protein release, rhNELL-1 was lyophilized onto apatite-coated β-TCP (aTCP) particles, as previously described (Supplemental Figure 1) (42). aTCP particles provide extended release kinetics of rhNELL-1 over unmodified β-TCP (42). Four spinal fusion sites per treatment group were randomly allocated to treatment groups as follows: (a) scaffold alone, consisting of DBX scaffold with PBS-loaded aTCP particles, (b) DBX with rhNELL-1–loaded aTCP particles (1.0 mg/ml rhNELL-1), and (c) DBX with rhNELL-1–loaded aTCP particles (1.7 mg/ml rhNELL-1). Spinal fusion contents are summarized in Table 1. Microparticle surface morphology was observed by scanning electron microscopy (SEM; JEOL JSM-6700). Before SEM analysis, samples were mounted on aluminum stubs and carbon coated. RhNELL-1 protein was produced by Aragen Bioscience.

Prior to surgical instrumentation, the release kinetics of rhNELL-1 from aTCP was assessed (Supplemental Figure 1). Ten micrograms of rhNELL-1 protein was lyophilized onto 50 mg of aTCP particles. The protein-adsorbed particles were immersed in 1 ml of 10 mM PBS (pH 7.4) at 37°C under gentle shaking. The particles were centrifuged for medium collection and the supernatant was replaced with 1 ml of fresh solution after 0, 1, 3, 5, 7, 10, and 14 days. The released protein was measured using the 3-(4-carboxybenzoyl)quinoline-2-carboxaldehyde protein assay (Invitrogen). Measurements were performed in triplicate and the amount of protein released was summed with the amount from previous time points and expressed as cumulative release.

For the surgical treatment allocation, block randomization was used to ensure equal treatment group sizes. Surgeons were completely blinded to treatment group. Briefly, a ventrolateral retroperitoneal approach to L3/L4 and L5/L6 was made through the oblique abdominal muscles to the plane ventral to the L3–L6 transverse processes. Using a vertebral spreader, the disc space was opened and the radiolucent cage (Vertebral Spacer-CR; Synthes) containing the treatment components was pressed into place. As the spinal fusion contents appeared visually identical between groups, no unblinding of the operating surgeons was observed. A 3-hole titanium plate was then applied on the dorsal surface of the operated vertebral bodies with 2 screws at the each end of the plate. The external abdominal muscular fascia and subcutaneous tissue were sutured for completion.

Nonhuman primate analyses. Analysis of nonhuman primate spinal fusion samples was performed by CT, microCT, FEA, histology, immunohistochemistry, and histomorphometry. Radiographs of the fusion sites were taken immediately prior to and after surgery for monitoring the cage position as well as at 2 and 3 months after surgery to follow the progression of the fusion. CT images were taken under general anesthesia. Successful spine fusion at the 3-month time point was defined as a 50% or greater area of contiguous bridging bone within the implant by radiographic evaluation. At 3 months, the L3/L4 and L5/L6 regions were removed after sacrifice and fixed in formaldehyde for subsequent analyses. Postmortem, high-resolution microCT scanning of individual spinal fusion segments was performed similarly to mouse studies. MicroCT quantitative analysis of the spinal fusion segment was performed postmortem. Measurements were made using an ROI of the spinal fusion segment, excluding native bone.

FEA (simulated biomechanical) was performed using microCT images converted to DICOM files using SKyScan Dicom Converter software. Tetrahedral 3D mesh models were created by drawing a random 2 × 2 × 2 mm cubic VOI within the spinal fusion segment, using ScanIP software. The selection was then segmented using Mimics' intensity threshold (range, 1,250–4,095) in Mimics software (version 16.0; Materialise, http://www.materialise.com). 3-matic (version 8.0; Materialise) was used to remesh these 3D mesh models with a shape quality threshold of 0.3 height/area, and a maximum triangle edge length of 0.1 mm. Following remeshing, the 3D cube models had an average of 271,000 elements. With the meshed models, FEA was performed using ABAQUS software. Material properties of the cancellous bone were assumed to be isotropic, homogeneous, and linearly elastic, with a Young's modulus of 3.5 GPa and a Poisson's ratio of 0.25 (23). Boundary conditions were set to encastre, constraining all translations and rotations on the lower (caudal) border nodes of the 3D cube

models. Next, we applied a uniaxial compressive stress force of 0.5 MPa on the superior surface of the 3D cubic VOIs to reproduce the physiologic, intradiscal pressure experienced in humans relaxed, standing to the upper (rostral) border nodes of the L4 vertebral body (43). Finally, the von Mises stress experienced by the samples was analyzed. All radiographic analyses, including ROI/VOI construction, were performed in a blinded fashion.

For histology, tissues were formalin fixed and either resin embedded for histology and histomorphometry, or paraffin embedded for immunohistochemistry. Histologic stains included H&E, GMT, and VKMT. Histological specimens were analyzed using an Olympus BX51 microscope and images acquired using a MicroFire digital camera with Picture Frame software. Histomorphometry was performed on serial VKMT-stained sections and are represented as percentage bone area, using 2–3 slides per sample and 3 random images per slide (4). Immunohistochemistry and semiquantitative analysis for CD31, CD45, and Sca-1 were performed as per mouse studies.

At 2 and 12 postoperative weeks, development of anti–NELL-1 IgG antibodies was assayed by serum ELISA measurements. RhNELL-1 protein was used as the antigen to coat 96-well polystyrene microtiter plates (1 μg/ml at a volume of 100 μl per well) by incubation overnight at 4°C. The plates were washed 5 times with PBS supplemented with 0.05% Tween-20 (PBST), and nonspecific binding was blocked with 100 μl per well of Tris-based diluents containing 1% BSA and 3% normal goat serum for 1 hour at room temperature. Plates were washed another 5 times and then 100 μl of diluted monkey serum (1:10) in Tris-based diluents from each treatment group was added. Negative control sera was collected from monkeys without any treatment. The plate was incubated for 1 hour at 37°C followed by 6 washes in PBST. HRP-conjugated goat anti-monkey IgG (1:50,000 and 1:100,000 dilution) or goat anti–rabbit IgG (1:50,000 and 1:100,000 dilution) was added at 100 μl per well and incubated for 30 minutes at 37°C. The plate was then washed 6 times in PBST, and a colorimetric reaction was developed with 100 μl/well of Vector Laboratories' Vectastain Universal Elite ABC Kit. After a 15-minute incubation in the dark at 37°C, the reaction was stopped by adding 50 μl per well of 4N H_2SO_4. The OD was measured with an ELISA microplate reader at 490 nm. All tests were carried out in duplicate.

Statistics. Quantitative data are expressed as the mean ± SEM unless otherwise described, with $*P < 0.05$ and $**P < 0.01$ considered significant. A Shapiro-Wilk test for normality was performed on all datasets. Homogeneity was confirmed by a comparison of variances test. Parametric data were analyzed using an appropriate 2-tailed Student's *t* test when 2 groups were being compared, or a 1-way ANOVA was used when more than 2 groups were compared, followed by a post-hoc Tukey's test to compare 2 groups. Nonparametric data were analyzed with a Mann-Whitney *U* test when 2 groups were being compared or a Kruskal-Wallis 1-way analysis when more than 2 groups were compared. Sample size calculations are as follows: for experiments presented in Figures 1–3, initial animal numbers were based on an $\alpha = 0.05$, power = 0.8, and an anticipated effect size of 3.73 (based on our previously published data in sheep spinal fusion) (27). For experiments presented in Figures 5 and 6, initial animal numbers were based on an $\alpha = 0.05$, power = 0.8, and an anticipated effect size of 2.69 (based on our previously published data in local rhNELL-1 injection in ovariectomized rats) (44). In vitro experiments were performed in biological triplicate, unless otherwise described. In vivo experiments were performed without replicate, unless otherwise described.

Study approval. All mice were cared for according to institutional guidelines set by the Chancellor's Animal Research Committee of the Office for Protection of Research Subjects at UCLA as well as the UCLA Office of Animal Research Oversight. All nonhuman primate care and surgical procedures were approved by the IULAC of Shandong University.

Author contributions

AWJ, JS, KT XZ, and CS designed the research study. AWJ, JS, RT, AN, KK, CAM, HCP, WL, JHK, and GA conducted experiments, acquired and analyzed data. ML conducted experiments, acquired and analyzed data, and provided reagents. AWJ, CTC, KT, XZ, and CS provided reagents. AWJ, JS, KT, XZ, and CS wrote the manuscript.

Acknowledgments

We would like to thank the following individuals and offices for their expertise: TPCL and Surgical Pathology divisions of the UCLA Department of Pathology and Laboratory Medicine. We thank Michael Chiang and Janette Zara for their excellent technical assistance. The authors thank Arthur A. Gertzman for the donation of demineralized bone graft products, and for his lifetime contributions to the field.

The present work was supported by the NIH/National Institute of Arthritis and Musculoskeletal and Skin (grant numbers R01 AR061399, R01 AR066782, and K08 AR068316), and the Orthopaedic Research and Education Foundation with funding provided by the Musculoskeletal Transplant Foundation.

Address correspondence to: Xinli Zhang, BOX 951668, 10833 Le Conte Ave., 30-121 CHS, Los Angeles, California 90095-1668, USA. Phone: 310.825.3750; Email: xzhang@dentistry.ucla.edu. Or to: Chia Soo, BOX 951759, 675 Charles E. Young Dr. South, Room 2641A, Los Angeles, California 90095-1759, USA. Phone: 310.794.5479; Email: bsoo@ucla.edu.

1. Ting K, et al. Human NELL-1 expressed in unilateral coronal synostosis. *J Bone Miner Res*. 1999;14(1):80–89.
2. Zhang X, et al. Craniosynostosis in transgenic mice overexpressing Nell-1. *J Clin Invest*. 2002;110(6):861–870.
3. Desai J, et al. Nell1-deficient mice have reduced expression of extracellular matrix proteins causing cranial and vertebral defects. *Hum Mol Genet*. 2006;15(8):1329–1341.
4. James AW, et al. NELL-1 in the treatment of osteoporotic bone loss. *Nat Commun*. 2015;6:7362.
5. Li CS, et al. Accelerated chondrogenic differentiation of human perivascular stem cells with NELL-1. *Tissue Eng Part A*. 2016;22(3–4):272–285.
6. Lee S, et al. Brief report: human perivascular stem cells and Nel-like protein-1 synergistically enhance spinal fusion in osteoporotic rats. *Stem Cells*. 2015;33(10):3158–3163.
7. Pang S, et al. Proliferation and osteogenic differentiation of mesenchymal stem cells induced by a short isoform of NELL-1. *Stem Cells*. 2015;33(3):904–915.
8. Cowan CM, et al. NELL-1 increases pre-osteoblast mineralization using both phosphate transporter Pit1 and Pit2. *Biochem Biophys Res Commun*. 2012;422(3):351–357.
9. Santamaría A, et al. Low-molecular-weight heparin, bemiparin, in the outpatient treatment and secondary prophylaxis of venous thromboembolism in standard clinical practice: the ESFERA Study. *Int J Clin Pract*. 2006;60(5):518–525.
10. Chen W, et al. Nfatc2 is a primary response gene of Nell-1 regulating chondrogenesis in ATDC5 cells. *J Bone Miner Res*. 2011;26(6):1230–1241.
11. Lee M, Siu RK, Ting K, Wu BM. Effect of Nell-1 delivery on chondrocyte proliferation and cartilaginous extracellular matrix deposition. *Tissue Eng Part A*. 2010;16(5):1791–1800.
12. Siu RK, et al. NELL-1 promotes cartilage regeneration in an in vivo rabbit model. *Tissue Eng Part A*. 2012;18(3–4):252–261.
13. Hasebe A, et al. The C-terminal region of NELL1 mediates osteoblastic cell adhesion through integrin α3β1. *FEBS Lett*. 2012;586(16):2500–2506.
14. Shen J, et al. NELL-1 promotes cell adhesion and differentiation via integrinβ1. *J Cell Biochem*. 2012;113(12):3620–3628.
15. Zhang X, et al. Nell-1, a key functional mediator of Runx2, partially rescues calvarial defects in Runx2 (+/-) mice. *J Bone Miner Res*. 2011;26(4):777–791.
16. Chen F, et al. NELL-1-dependent mineralisation of Saos-2 human osteosarcoma cells is mediated via c-Jun N-terminal kinase pathway activation. *Int Orthop*. 2012;36(10):2181–2187.
17. Bokui N, et al. Involvement of MAPK signaling molecules and Runx2 in the NELL1-induced osteoblastic differentiation. *FEBS Lett*. 2008;582(2):365–371.
18. Shen J, et al. Novel Wnt regulator NEL-like molecule-1 antagonizes adipogenesis and augments osteogenesis induced by bone morphogenetic protein 2. *Am J Pathol*. 2016;186(2):419–434.
19. Aghaloo T, et al. Nell-1-induced bone regeneration in calvarial defects. *Am J Pathol*. 2006;169(3):903–915.
20. Li W, et al. Delivery of lyophilized Nell-1 in a rat spinal fusion model. *Tissue Eng Part A*. 2010;16(9):2861–2870.
21. Li W, et al. Nell-1 enhances bone regeneration in a rat critical-sized femoral segmental defect model. *Plast Reconstr Surg*. 2011;127(2):580–587.
22. Siu RK, et al. Nell-1 protein promotes bone formation in a sheep spinal fusion model. *Tissue Eng Part A*. 2011;17(7–8):1123–1135.
23. Lu SS, et al. The osteoinductive properties of Nell-1 in a rat spinal fusion model. *Spine J*. 2007;7(1):50–60.
24. van de Rijn M, Heimfeld S, Spangrude GJ, Weissman IL. Mouse hematopoietic stem-cell antigen Sca-1 is a member of the Ly-6 antigen family. *Proc Natl Acad Sci U S A*. 1989;86(12):4634–4638.
25. Spangrude GJ, Heimfeld S, Weissman IL. Purification and characterization of mouse hematopoietic stem cells. *Science*. 1988;241(4861):58–62.
26. Bonyadi M, Waldman SD, Liu D, Aubin JE, Grynpas MD, Stanford WL. Mesenchymal progenitor self-renewal deficiency leads to age-dependent osteoporosis in Sca-1/Ly-6A null mice. *Proc Natl Acad Sci U S A*. 2003;100(10):5840–5845.
27. Guo Z, et al. In vitro characteristics and in vivo immunosuppressive activity of compact bone-derived murine mesenchymal progenitor cells. *Stem Cells*. 2006;24(4):992–1000.
28. Wu X, et al. Inhibition of Sca-1-positive skeletal stem cell recruitment by alendronate blunts the anabolic effects of parathyroid hormone on bone remodeling. *Cell Stem Cell*. 2010;7(5):571–580.
29. Stanford WL, et al. Altered proliferative response by T lymphocytes of Ly-6A (Sca-1) null mice. *J Exp Med*. 1997;186(5):705–717.
30. Ito CY, Li CY, Bernstein A, Dick JE, Stanford WL. Hematopoietic stem cell and progenitor defects in Sca-1/Ly-6A-null mice. *Blood*. 2003;101(2):517–523.
31. Yuan W, et al. NELL-1 based demineralized bone graft promotes rat spine fusion as compared to commercially available BMP-2 product. *J Orthop Sci*. 2013;18(4):646–657.
32. Jin Z, et al. Hypermethylation of the nel-like 1 gene is a common and early event and is associated with poor prognosis in early-stage esophageal adenocarcinoma. *Oncogene*. 2007;26(43):6332–6340.
33. Mori Y, et al. A genome-wide search identifies epigenetic silencing of somatostatin, tachykinin-1, and 5 other genes in colon

cancer. *Gastroenterology*. 2006;131(3):797–808.
34. Shen J, et al. NELL-1 expression in tumors of cartilage. *J Orthop*. 2015;12(Suppl 2):S223–S229.
35. Shen J, et al. NELL-1 expression in benign and malignant bone tumors. *Biochem Biophys Res Commun*. 2015;460(2):368–374.
36. Nakamura R, Nakamoto C, Obama H, Durward E, Nakamoto M. Structure-function analysis of Nel, a thrombospondin-1-like glycoprotein involved in neural development and functions. *J Biol Chem*. 2012;287(5):3282–3291.
37. Askarinam A, et al. Human perivascular stem cells show enhanced osteogenesis and vasculogenesis with Nel-like molecule I protein. *Tissue Eng Part A*. 2013;19(11–12):1386–1397.
38. Parfitt AM, et al. Bone histomorphometry: standardization of nomenclature, symbols, and units. Report of the ASBMR Histomorphometry Nomenclature Committee. *J Bone Miner Res*. 1987;2(6):595–610.
39. Klinck J, Boyd SK. The magnitude and rate of bone loss in ovariectomized mice differs among inbred strains as determined by longitudinal in vivo micro-computed tomography. *Calcif Tissue Int*. 2008;83(1):70–79.
40. Buie HR, Moore CP, Boyd SK. Postpubertal architectural developmental patterns differ between the L3 vertebra and proximal tibia in three inbred strains of mice. *J Bone Miner Res*. 2008;23(12):2048–2059.
41. Bouxsein ML, Myers KS, Shultz KL, Donahue LR, Rosen CJ, Beamer WG. Ovariectomy-induced bone loss varies among inbred strains of mice. *J Bone Miner Res*. 2005;20(7):1085–1092.
42. Hu J, Hou Y, Park H, Lee M. Beta-tricalcium phosphate particles as a controlled release carrier of osteogenic proteins for bone tissue engineering. *J Biomed Mater Res A*. 2012;100(7):1680–1686.
43. Kuo CS, et al. Biomechanical analysis of the lumbar spine on facet joint force and intradiscal pressure--a finite element study. *BMC Musculoskelet Disord*. 2010;11:151.
44. Kwak J, et al. NELL-1 injection maintains long-bone quantity and quality in an ovariectomy-induced osteoporotic senile rat model. *Tissue Eng Part A*. 2013;19(3–4):426–436.